Fe₃S₄ nanoparticles for arterial inflammation therapy: Integration of magnetic hyperthermia and photothermal treatment

Junchao Liu [a,1], Xin Guo [a,1], Zhen Zhao [a,1], Bo Li [a,*], Jinbao Qin [a], Zhiyou Peng [a], Guanjie He [b],
Dan J.L. Brett [b], Ruihua Wang [a,*], Xinwu Lu [a,c,*]

[a] Department of Vascular Surgery, Shanghai Ninth People's Hospital, Shanghai JiaoTong University School of Medicine, Shanghai, 200011, PR China
[b] Department of Chemical Engineering, University College London, London, WC1E 7JE, UK
[c] Vascular Center of Shanghai JiaoTong University, Shanghai, 200011, PR China

ARTICLE INFO

ABSTRACT

Photothermal therapy (PTT), based on nanoparticles, has been widely explored in the treatment of multiple diseases. However, limited by laser penetration ability, its treatment efficiency can be reduced when treating deep arterial inflammation, which is the major cause of atherosclerosis and vessels stenosis. Magnetic hyperthermia (MHT) has the outstanding tissue permeability, while its magnetothermal efficiency was relatively poor. In this study, Fe₃S₄ nanoparticles (NPs) were synthesized and characterized, and its dual capacity to convert light and magnetic stimulation into heat was confirmed. The Fe₃S₄ NPs also presented superior biocompatibility and great T2 weighted magnetic resonance imaging properties ($52.8\,\mathrm{mM}^{-1}\,\mathrm{S}^{-1}$). Besides, its excellent effect in ablating inflammatory macrophages combining PTT and MHT was verified *in vitro*. *In vivo* experiment on Apo E-/- mice models exhibited that PTT combined with MHT could effectively eliminate infiltrating inflammatory macrophages and further inhibit the formation of arterial stenosis. This study concludes that the integration of PTT and MHT based on Fe₃S₄ NPs can serve as an effective therapeutic strategy for the treatment of atherosclerosis and vessels stenosis.

© 2019 The Author(s). Published by Elsevier Ltd. This is an open access article under the CC BY license (http://creativecommons.org/licenses/by/4.0/).

1. Introduction

Atherosclerosis is one of the top health problems affecting human worldwide and it is the main cause of many vascular diseases. Large numbers of patients die from vascular diseases every year, and this trend is on the rise [1,2]. Recently, it has been demonstrated that atherosclerosis is essentially an inflammatory process, in which macrophages play important roles, especially in the course of initiation, growth and eventual rupture of arterial plaques [3–5]. Besides, the major way in clinic to treat atherosclerosis is balloon dilatation and stent implantation, which can relieve ischemic symptoms temporarily but also activate macrophages to cause inflammation at the same time. As a result, various cytokines were released by those activated macrophages, leading to the proliferation of smooth muscle cells (SMCs) and eventually vessels restenosis [6–8]. Therefore, eliminating local aggregation of inflammatory macrophages can be an effective approach to inhibit atherosclerosis and vessels stenosis.

As non-invasive and safe therapeutic agents, nanomaterials have been widely used in biotherapeutic research for various diseases, especially in cancer therapy [9–15]. Hyperthermia based on nanomaterials can be divided into two categories: magnetic hyperthermia (MHT) and photothermal therapy (PTT). Owing to the outstanding photothermal conversion efficiency of PTT, nanomaterials such as metal compounds [16–20], chalcogenides [21,22] and pyroelectric materials [23] have shown superiority in destroying surface tumor cells. However, limited by laser penetration ability, PTT exhibits disadvantages in the treatment of deep lesions. MHT, generating from an alternating magnetic field, has the advantage of tissue penetration, and it can be used without depth limitation [24–27]. However, the heat yield per nanoparticle by MHT was much less than that of PTT. Therefore, combining MHT and PTT means producing cumulative heating in targeted sites by exploiting inherent advantages and overcoming respective limitations. Many preliminary researches have confirmed its superiority in the treatment of deep lesions [28–31]. Our previous studies have found that photothermal nanomaterials can eliminate inflammatory macrophages around the arterial wall to some extent [32–34],

* Corresponding authors at: Department of Vascular Surgery, Shanghai Ninth People's Hospital, Shanghai JiaoTong University School of Medicine, Shanghai, 200011, PR China.
E-mail addresses: boli@shsmu.edu.cn (B. Li), wangruihua0330@sina.com (R. Wang), luxinwu@shsmu.edu.cn (X. Lu).
[1] These authors contributed equally to this work.

but due to the deep position of arteries, the laser may be partially absorbed by the surrounding tissues during treatment, thus reducing its therapeutic effect in treating deep artery inflammation. Therefore, taking advantages of PTT and MHT simultaneously may achieve better results in the treatment of arterial inflammatory. In order to produce enough magnetic hyperthermia in deep position, a relatively high administered dose is needed, which requires nanomaterials have the property of good biocompatibility. Since iron is an important component of hemoglobin and is abundant in human body, iron nanoparticles are considered to be more biocompatible than other metal elements (Cu, Mo). Previous studies have shown that iron-based agents, such as FeS and FeS_2 nanomaterials, have good photothermal conversion efficiency and magnetic properties [35–37].

In this study, Fe_3S_4 nanoparticles (Fe_3S_4 NPs) were synthesized, and their characterization and photothermal and magnetothermal properties were evaluated. The cytotoxicity, PTT and MHT effect of Fe_3S_4 NPs on macrophages were assessed in vitro. During in vivo experiment, Apo E knockout mice were used to construct arterial inflammation models and PTT combining MHT therapy based on the local injection of Fe_3S_4 NPs were subsequently carried out. The Fe_3S_4 NPs also presented great T2 weighted magnetic resonance imaging properties. Histological analysis was conducted to evaluate the effect of PTT combined with MHT in preventing the occurrence of atherosclerosis and stenosis. The specific mechanism of arterial inflammation therapy using PTT and MHT was illustrated in Scheme 1. As far as we know, this is the first research to eliminate arterial inflammation using combined PTT and MHT approaches, which may provide a new therapeutic method for the treatment of atherosclerosis and vessels stenosis.

2. Experiment section

2.1. Materials

Raw264.7, mouse macrophage cell line, was purchased from the Shanghai Cell Bank, the Chinese Academy of Sciences (Shanghai, China). Dulbecco's modified Eagle's medium (DMEM, with high glucose), fetal bovine serum (FBS, Waltham, MA, USA), Trypsin-EDTA (0.25%), penicillin/streptomycin were purchased from Gibco (Carlsbad, CA, USA). Primary antibodies, including F4/80, CD68, CD11b and secondary antibodies were purchased from Abcam (Cambridge, MA, USA). The Cell Counting Kit-8 (CCK-8) and Calcein-AM/PI Double Stain Kit were obtained from Dojindo (Kumamoto, Japan). Other chemical reagents were obtained from Shanghai Chemical Reagent Research Institute Co. Ltd (Shanghai, China) and used according to manufacturer's instructions.

2.2. Synthesis and characterization of Fe₃S₄ NPs

$FeSO_4·7H_2O$ (1 mmol), L-Cysteine (1 mmol) and poly (vinyl pyrrolidone) (PVP, K30) were mixed together and dissolved in 30 mL of deionized (DI) water under vigorous magnetic stirring. Then, 100 μL ethylenediamine was added into the above solution. Finally, the resulting solution was transferred to a stainless steel autoclave, sealed, and heated at 200 °C for 24 h. A black precipitate was collected by centrifugation and washed with ethanol and DI water several times.

Transmission electron microscopy (TEM) images were taken on a transmission electron microscope (TEM-2010F). UV–vis-NIR absorbance spectra were obtained at room temperature using a UV–vis-NIR spectrophotometer (UV-1902PC, Phenix). X-ray diffraction (XRD) measurement was performed with a D/max-2550 PC X-ray diffractometer (Rigaku). X-ray photoelectron spectra (XPS) analyses were conducted using an ESCA-Lab 250Xi (Thermo

Scientific) spectrometer. The concentration of iron ions was measured by an inductively coupled plasma atomic emission spectroscopy (ICP-AES; Leeman Laboratories Prodigy). The 915 nm semiconductor lasers were purchased from Shanghai Xilong Optoelectronics Technology Co. Ltd., China, whose power could be adjusted externally (0–2 W). The output power of lasers was independently calibrated using a hand-held optical power meter (Newport model 1918-C, CA, USA).
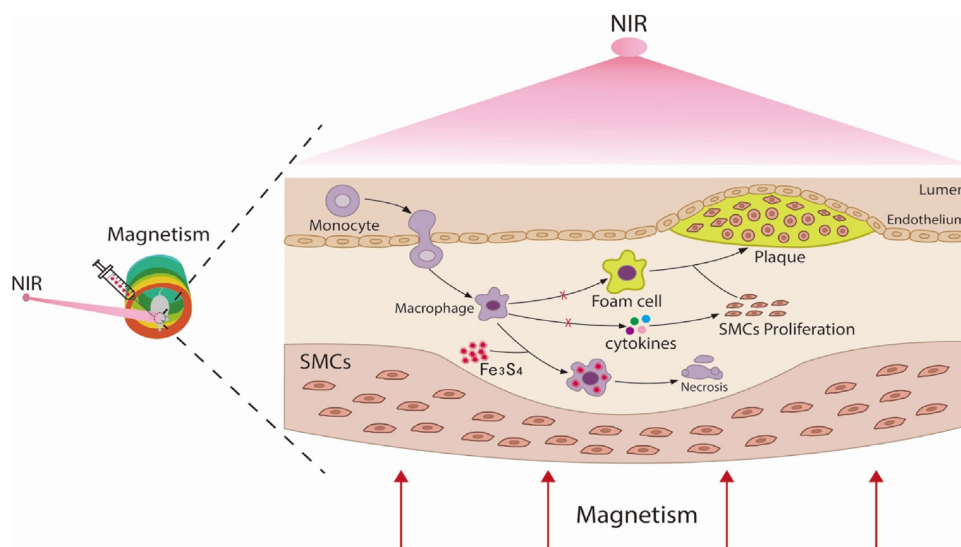
A thermal imaging camera (GX-300; Shanghai Infratest Electronics Co., Ltd, China) was used to monitor temperature change in real time, every five seconds. To measure the photothermal performance, the solution (100 μL) of Fe_3S_4 NPs with various concentrations was irradiated by the 808 nm semiconductor laser devices at the indicated power density for 5 min. The working distance was 10 cm and a spot area was ∼ 0.316 cm². To record the magnetic hyperthermia effect of the Fe_3S_4 NPs dispersions, 100 μL of aqueous dispersions were conducted on foamed plastic in inductive coils using an AC magnetic field induction system. The magneto-optical performance of Fe_3S_4 NPs (500 μg mL⁻¹, 100 μL) was assessed under the simultaneous stimulation including an 808 nm laser irradiation at the safe power (0.3 W cm⁻²) and a physiologically safe range of AC magnetic field (< 5 × 10⁹ A m⁻¹ s⁻¹) for 5 min.

2.3. Cell culture and characterization

Mouse macrophage cell line Raw264.7, purchased from the Shanghai Cell Bank, the Chinese Academy of Sciences (Shanghai, China), was cultured in Dulbecco's Modified Eagle's Medium (DMEM, with 4500 mg L⁻¹ glucose), which was supplemented with 10% fetal bovine serum (FBS, Waltham, MA, USA) and 1% streptomycin/penicillin (Sigma, St. Louis, MO). The culture condition was controlled at 37 °C in a humidified 5% CO₂ atmosphere. In order to identify Raw 264.7 macrophage properties, flow cytometry and cellular immunofluorescence experiments were performed. For flow cytometry analysis, specific surface markers of macrophages, CD68 and F4/80 were examined. In immunofluorescence experiments, surface protein marker CD68 was stained. Then a fluorescence microscope (Olympus, Japan) and a flow cytometer (Beckman Coulter, Fullerton, CA) were separately used to detect the targeted markers.

2.4. Cytotoxicity, cell viability assay and intracellular TEM

To evaluate the cytotoxicity of Fe_3S_4 NPs, Raw264.7 was seeded in 96-well plates and co-cultured with different concentrations (0, 100, 300, 500, 800, 1000 μg mL⁻¹) of Fe_3S_4 NPs for 12 h. Cell viability was measured by CCK-8 cell proliferation assay according to the manufacturer's instructions. Then the safe concentration was confirmed and used for the follow-up experiment. To evaluate the photothermal, magnetic, or the combined effects on Raw264.7, a suitable concentration of Fe_3S_4 NPs was co-cultured with Raw264.7 for 12 h and those cells were subjected to an 808 nm NIR laser irradiation, AC magnetic field, combined therapy for 5 min or not. After which, the treated cells were stained with calcein AM/PI (Dojindo Laboratories, Shanghai, China) to observe living cells (Calcein AM, green fluorescence) and dead cells (PI, red fluorescence) under the immunofluorescence microscope. Besides, the cell apoptosis assay was performed using flow cytometry after Annexin V/PI (Dojindo Laboratories, Shanghai, China) staining. For the intracellular TEM assay, those cells at different groups were collected, and subsequent experiments were performed following the procedures described previously.

Scheme 1. The schematic illustration of arterial inflammation therapy using magnetic hyperthermia and photothermal therapy simultaneously.

2.5. Magnetic resonance imaging

A small animal MR scanner (MesoMR23-060H-I) was used to scan the Fe_3S_4 NPs dispersions at different Fe concentrations (0–0.28 mM). All procedures were performed at room temperature using a spin echo sequence and the parameters is TR/TE = 300/20 ms, repetition time 3. The Fe_3S_4 NPs (100 μL, 500 μg mL^{-1}) per mouse were injected around the left carotid artery under the guidance of ultrasound and the mice were scanned with the same MR scanner before and after the injection. During the process, the mice were deeply anesthetized to avoid the interference caused by unintentional movement of the mice.

2.6. Animal preparation for photothermal therapy and magnetic hyperthermia

All animal experiments were processed under the protocols approved by Animal Care and Use Committee of Shanghai Ninth People's Hospital, Shanghai Jiao Tong University, School of Medicine. 8-week old male Apo E knocked mice were purchased from the Shanghai Research Center for Model Organisms (Shanghai, China) and fed with high-fat diet (21% fat, 0.15% cholesterol) in a specific pathogen-free environment. The animal models of atherosclerosis were prepared as before. 28 mice were anaesthetized with phenobarbital sodium (40 mg kg^{-1}) by intraperitoneal injection. The left carotid arteries were exposed and sheathed with a contractile silicon tube, as described previously. After 14 days, Fe_3S_4 NPs (500 μg mL^{-1}, 100 μL), dissolved in PBS was injected into the left carotid arteries of 21 mice under ultrasound guidance, while another 7 mice were injected with an equivalent volume of PBS as the control group. Those mice injected with Fe_3S_4 NPs were randomly divided into 3 groups according to different treatments: photothermal therapy group (Fe_3S_4+PTT), magnetic hyperthermia group (Fe_3S_4+MHT), and photothermal therapy combined with magnetic hyperthermia group (Fe_3S_4+PTT + MHT). After 12 h, those three groups were separately exposed to 808 nm laser at the power density of 0.3 W cm^{-2}, moderate radio frequency of 595 kHz and a current of 14.5 kA magnetic field strength, or the combination of both for 5 min separately. GX-300 photothermal medical device (Shanghai Infratest Electronics Co., Ltd, China) was used to record the temperature of the left carotid artery dynamically.

2.7. Histological analysis and blood examination

On the 28th day after operation, mice in all groups were sacrificed, and the left carotid arteries were obtained. After which, the vessels were stained by immunofluorescence (CD68 for macrophage, SMA for SMC, DAPI for nuclei) and the relative numbers of macrophages around vessels were counted. Besides, HE stain was used to determine the thickness of the intima and media of vessels. In order to assess the biocompatibility and toxicity of Fe_3S_4 NPs *in vivo*, the major viscera (heart, liver, spleen, lung, kidney, intestine) were made into sections for haematoxylin/eosin (HE) staining and their morphological changes were observed. To measure the distribution of Fe_3S_4 *in vivo*, the main organs of mice in Fe_3S_4 group and PBS group were dissected on the 1st, 3rd, 7th, 14th day post injection. Iron concentrations in different organs were then examined using ICP-AES analysis. Besides, the blood samples of mice in both groups at the timepoints of 3, 7, 14 days after injection were also collected, and important biochemical parameters were measured.

2.8. Statistics

Quantitative data was described as means ± standard deviation, and comparisons among groups were analyzed by one-way analysis of variance. P-value < 0.05 was defined as statistically significant. The comparison results were labeled with * for P-value < 0.05, ** for P-value < 0.01 and *** P-value < 0.001.

3. Results and discussion

3.1. Synthesis and characterization of Fe_3S_4 NPs

Hydrophilic Fe_3S_4 NPs were prepared by a facile one-pot hydrothermal synthesis method in the presence of poly-vinyl-pyrrolidone (PVP). TEM shows good mono-dispersity of the resulting Fe_3S_4 NPs (Fig. 1A). Further investigation of microstructure information of the as-synthesized NPs was obtained from the high-resolution transmission electron microscope (HRTEM) image. The HRTEM image (Fig. 1B) shows a single crystal with an interplanar spacing of 0.298 nm, which corresponds to the d-spacing for (311) planes of Fe_3S_4 crystal. According to the TEM images, the size of Fe_3S_4 NPs was found to be 13 nm (Fig. 1C). The size is much smaller than those previously reported nanomaterials using a simi-
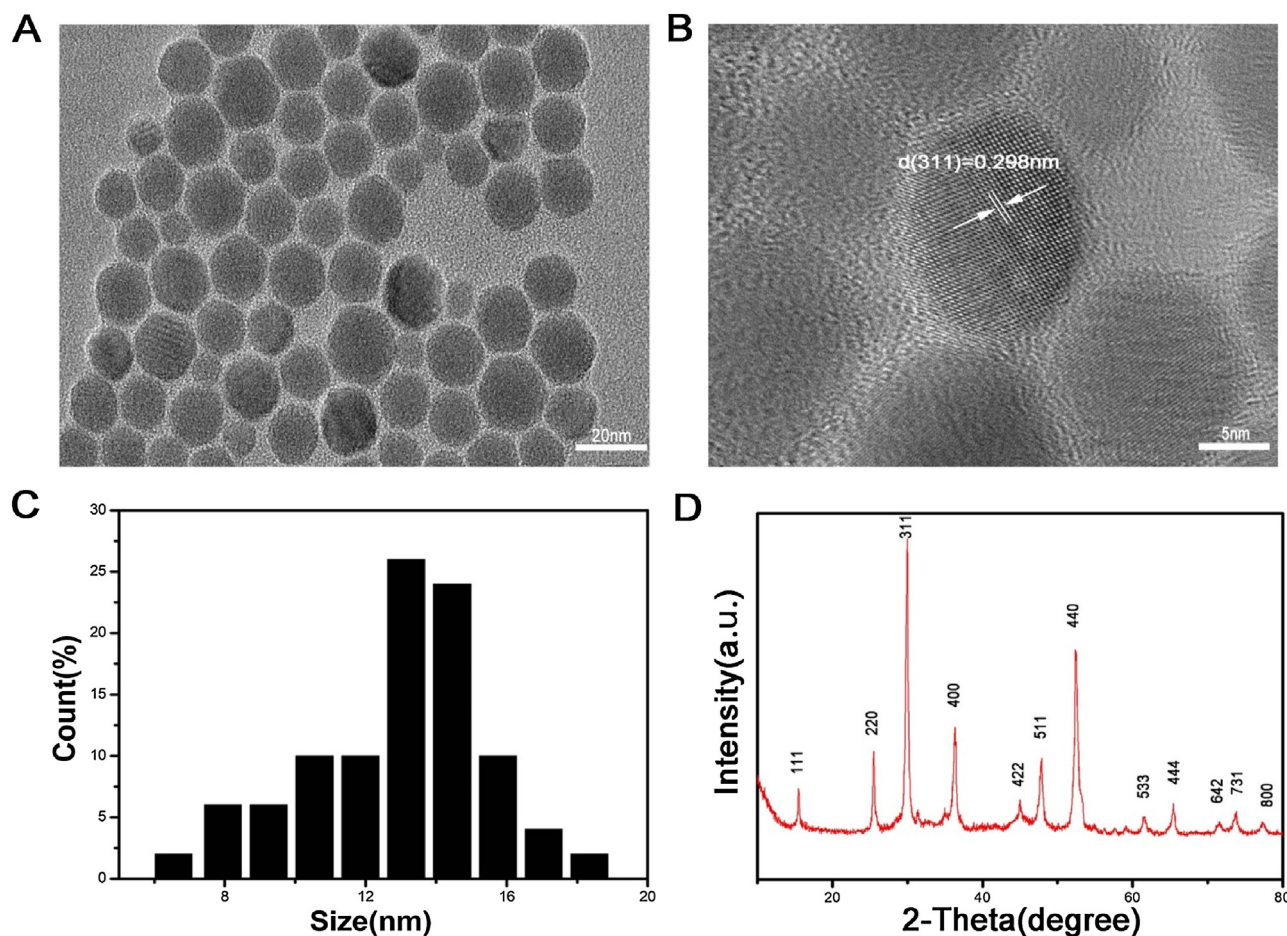
Fig. 1. Characterization of the Fe_3S_4 NPs. (A) TEM image of the Fe_3S_4 NPs. (B) High magnification of image (A). (C) Size distribution of Fe_3S_4 NPs in aqueous solution. (D) XRD pattern of Fe_3S_4 NPs.

lar synthetic method. This effective particle size reduction resulted from the presence of ethylenediamine, as demonstrated in our previous work on ultrasmall $CuCo_2S_4$ NPs. As illustrated in Fig. 1D, all of the X-ray diffraction (XRD) peaks of the Fe_3S_4 NPs could be well indexed as greigite Fe_3S_4 NPs, with lattice parameters matched well with those on JCPDS file (card no. 16-0713), indicating the formation of the pure phase Fe_3S_4 with high crystallinity.

The composition and chemical bonding state of the Fe_3S_4 NPs were performed by X-ray photoelectron spectroscopy (XPS, Figure S1 in the Supporting Information), showing that the as-prepared sample is mainly composed of Fe and S elements without other obvious impurities (the C and O peaks originate from the ligands). Fig. 2A shows high-resolution XPS analysis of Fe 2p of the NPs. The two peaks at 712 eV and 725 eV correspond to Fe^{3+} ions, and the other two peaks at 710.5 eV and 724.0 eV were assigned to Fe^{2+} species, indicating the coexistence of Fe^{3+} and Fe^{2+} in as-prepared Fe_3S_4 NPs. Also, the ratio of Fe to S in Fe_3S_4 NPs was determined to be 0.68, which is less than 3/4. These results confirmed the presence of large numbers of metal defects, which could contribute to the NIR absorption of Fe_3S_4 NCs. To verify the hypothesis, the optical properties of Fe_3S_4 NPs were measured. Fig. 2B shows the UV–vis spectra of the Fe_3S_4 NPs. As expected, the aqueous dispersion of Fe_3S_4 NPs showed strong absorption from visible to NIR region. Besides, the zeta potential of Fe_3S_4 NPs (500 μg mL^{-1}) was recorded for 5 min using zeta potential analyser (Nicomp Z3000), and the result showed that the average zeta potential value was -1.67 mV (Fig. S2). Greigite Fe_3S_4 is a counterpart of magnetite (Fe_3O_4). Although

Fe_3S_4 nanoparticles can be synthesized by various techniques, the magnetic thermal performance of these materials has been seldom investigated. Thus, the magnetically induced heating efficiency of the aqueous suspensions of Fe_3S_4 NPs was further studied. 0.1 mL of aqueous solutions at the varied concentration were placed inside an AC magnetic field with a moderate radio frequency of 595 kHz and a current of 14.5 kA. As shown in Fig. 3A, Fe_3S_4 NPs exhibited a concentration-dependent magnetic thermal effect. As a control experiment, the temperature of pure water showed little change. As seen, the temperature elevation of aqueous suspension at a concentration of 500 μg mL^{-1} reached 13 °C (Fig. 3A and D), which is enough to inhibit macrophage proliferation. The photothermal performance of Fe_3S_4 NPs aqueous suspension (500 μg mL^{-1}) under the irradiation of an 808 nm laser with varied power densities was further investigated. As shown in Fig. 3B, the Fe_3S_4 NPs exhibited an excellent photothermal effect due to the strong NIR absorption. According to the results from Fig. 3B and E, the power density was optimized to be 0.3 W cm^{-2}. The photo-magnetic thermal performance of Fe_3S_4 NPs (500 μg mL^{-1}) under the simultaneous stimulation including an 808 nm laser irradiation at the safe power (0.3 W cm^{-2}) and a physiologically safe range of AC magnetic field was further investigated. It was found that the temperature elevation could reach by 22.5 °C (Fig. 3C and F). Therefore, Fe_3S_4 NPs exhibited great potential for photo-magnetic hyperthermia therapy of arterial inflammation.

In addition, phantom images of Fe_3S_4 NPs dispersion with different Fe concentrations (0-0.30 mM) were examined using a
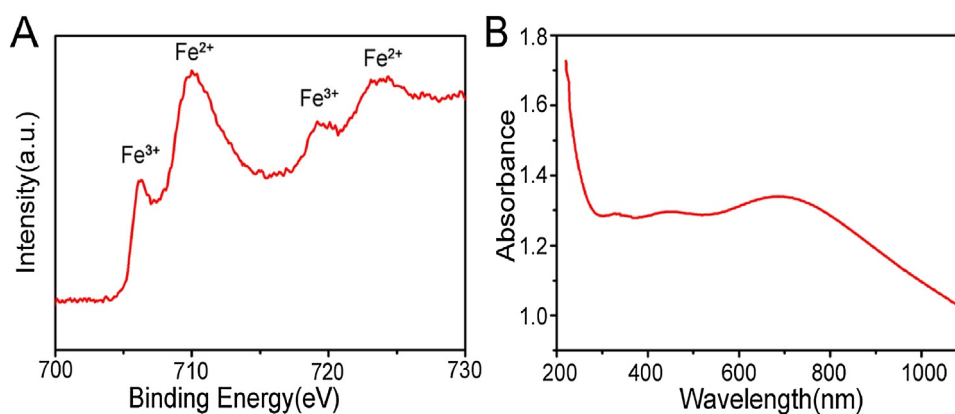
Fig. 2. (A) XPS spectra of Fe 2p, and Fe 3p. (B) UV–vis-NIR absorption spectra of the Fe_3S_4 NPs at room temperature.
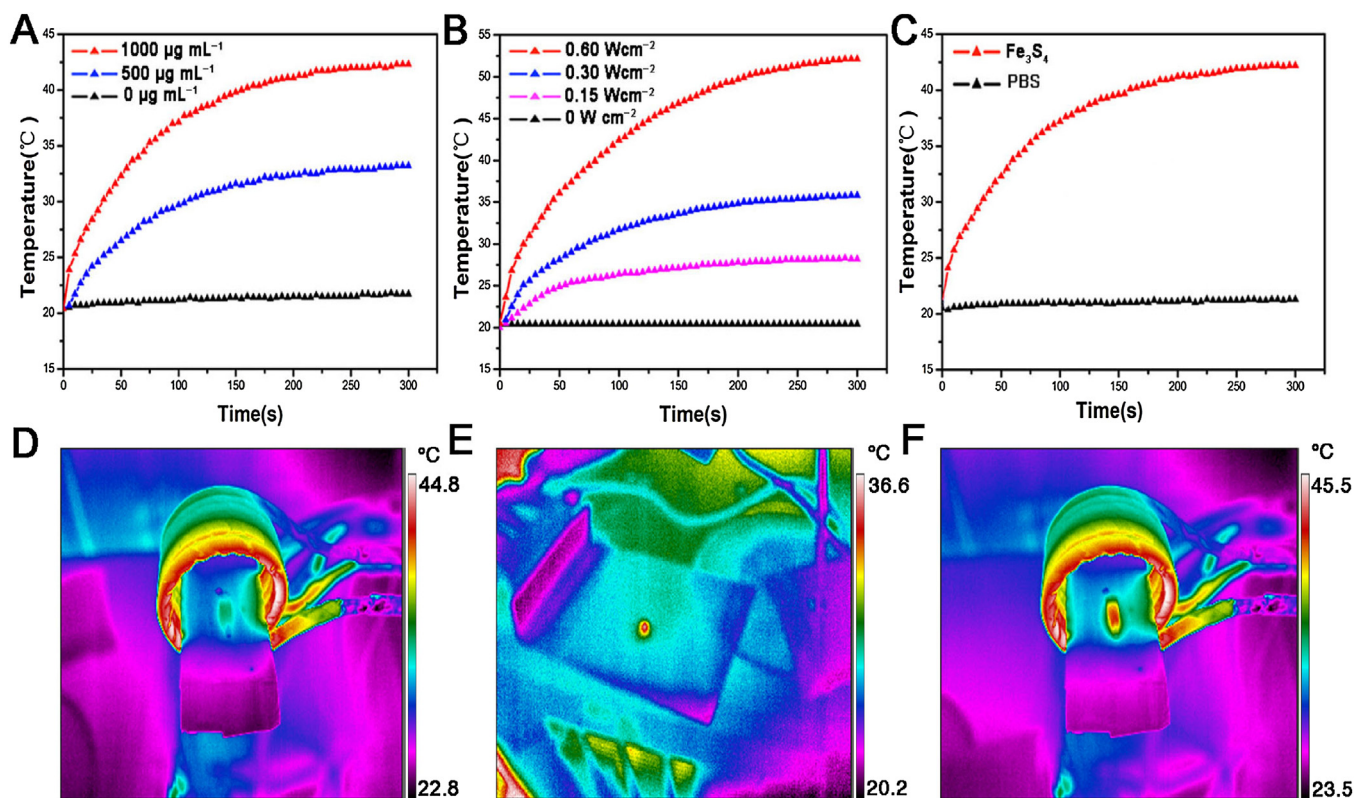

Fig. 3. (A) Magnetothermal effect of Fe_3S_4 NPs at different concentration (0, 500, 1000 $\mu g\,mL^{-1}$). (B) Photothermal effect of Fe_3S_4 NPs at the concentration of 500 $\mu g\,mL^{-1}$ with 808 nm NIR laser irradiation under different power density (0, 0.1, 0.3, 0.6 $W\,cm^{-2}$). (C) Combined effect of Fe_3S_4 NPs at the concentration of 500 $\mu g\,mL^{-1}$ under the power density of 0.3 $W\,cm^{-2}$ and AC magnetic field (595 kHz, 14.5 kA) simultaneously. (D) Representative magnetothermal image of (A). (E) Representative photothermal image of (B). (F) Representative photo-magnetic hyperthermia image of (C).

0.5 T MR scanner. As shown in Fig. 4A, as the Fe concentrations increased, the T2-weight image showed a noticeable darkening effect. Based on the results, we calculated the transverse relaxivity (r2) value of the Fe_3S_4 NPs and it was shown to be 52.8 $mM^{-1}\,S^{-1}$, which exhibited that the Fe_3S_4 NPs were an effective MRI contrast agent (Fig. 4B). Then animal experiments were carried out to examine the contrast effect of Fe_3S_4 NPs *in vivo*. After the injection of Fe_3S_4 NPs around left carotid artery of a mouse, the image of left neck became darker compared with that before injection (Fig. 4C). The results demonstrated that Fe_3S_4 NPs had excellent contrast effect for T2-weighted MRI both *in vivo* and *in vitro* and could be an ideal candidate for image-guided treatment.

3.2. The cytotoxicity, photothermal and magnetothermal effects on macrophages *in vitro*

Raw264.7 used in this work is a mouse macrophage cell line, which owns the characteristics of rapid growth and strong phagocytosis. Therefore, it has been widely applied for the study of macrophage's function and characteristics. Raw264.7 was investigated by flow cytometry and cellular immunofluorescence to analyze the specific protein markers of macrophage. Cellular immunofluorescence (Fig. S3A) demonstrated that Raw264.7 was positive for CD68 (red), with nuclear staining with DAPI (blue). In addition, flow cytometry analysis showed that Raw264.7 were strongly positive for F4/80 (94.7% ± 1.37%, Fig. S3B) and CD68
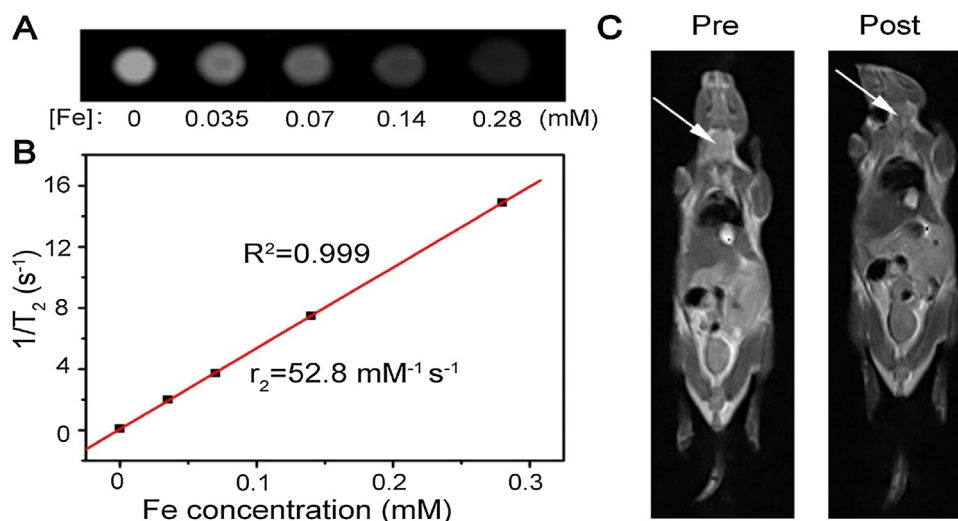
Fig. 4. (A) The T2-weighted MRI signals intensity of different Fe concentration (0–0.28 mM) *in vitro*. (B) The transverse relaxation rate of Fe_3S_4 NPs. (C) The MRI image of a mouse before and after the injection of Fe_3S_4 NPs around carotid artery.

(90.1% ± 2.5%, Fig. S3C), which were both macrophage surface antigens. The cytotoxicity of Fe_3S_4 NPs should be assessed before any biomedical applications. After co-culturing with Fe_3S_4 NPs for 12 h, the CCK-8 assay was used to detect the concentration-dependent effect of Fe_3S_4 NPs on Raw264.7. The results showed that no significant difference was observed in cell viability and cell morphology between the Fe_3S_4 NPs groups and the control group at the concentrations under $500\,\mu g\,mL^{-1}$. When the concentration reached $800\,\mu g\,mL^{-1}$, the viability of Raw264.7 was slightly affected (Fig. 5A). Those results showed that Fe_3S_4 NPs exhibited good biocompatibility at the concentration below $500\,\mu g\,mL^{-1}$. Considering the magnetothermal curve and photothermal curve of Fe_3S_4 NPs described above, $500\,\mu g\,mL^{-1}$ was chosen as the concentration used in the experiment. Owing to the decrease of laser penetration, low-laser power ($0.3\,W\,cm^{-2}$) was used to mimic the treatment process *in vivo*.

To study the thermal effect of Fe_3S_4 NPs on macrophages, Raw264.7 was co-culturing with Fe_3S_4 NPs of $500\,\mu g\,mL^{-1}$ for 12 h and then exposed to 808 nm laser ($0.3\,W/cm^2$), AC magnetic field (595 kHz, 14.5 kA) or both for 5 min, separately. Subsequently, Raw264.7 cells were stained with Calcein AM/PI for living cells (green)/dead cells (dead), and then observed under a fluorescence microscope. Cell viability was also quantitatively evaluated using a CCK-8 assay. Calcein AM/PI results (Fig. 5C) showed that almost no dead cells were seen in the control group, PTT + MHT group and Fe_3S_4 group. However, about 50% cells were killed in Fe_3S_4+PTT group and Fe_3S_4+MHT group, while more than 90% cells in Fe_3S_4+PTT + MHT group were dead. The CCK-8 assay performed a consistent result with the Calcein AM/PI ((Fig. 5B). Morphological changes may occur during the process of apoptosis, including cell lysis, cell shrinkage, nuclear pyknosis, nuclear fragmentation, nuclear dissolution *etc* [38–40]. Therefore, TEM was used to identify the phagocytosis of macrophages towards Fe_3S_4 NPs and the state of macrophages. After co-culturing with Fe_3S_4 NPs of $500\,\mu g\,mL^{-1}$ for 12 h, Raw264.7 exhibited good phagocytosis, and no significant damage was found within cells (Fig. 6A a). However, Nuclear pyknosis was observed in Raw264.7 after exposed to AC magnetic field for 5 min and cell shrinkage and nuclear fragmentation were noticed after irradiated with an 808 nm laser for 5 min (Fig. 6A b and c). Moreover, significant nuclear solubilization and cell lysis were observed in those cells after exposure to 808 nm laser irradiation and AC magnetic field for 5 min simultaneously (Fig. 6A d). Flow cytometry analysis showed that compared with Fe_3S_4 group

(7.35 ± 1.45%), Fe_3S_4+ MHT group (32.36 ± 8.60%) and Fe_3S_4+PTT group (40.53 ± 6.45%), a significantly higher apoptosis index was found in Fe_3S_4+PTT + MHT group (74.56 ± 9.15%). Those results demonstrated that combining PTT and MHT of Fe_3S_4 NPs could eliminate macrophages effectively and may have great potentials to alleviate chronic arterial inflammation.

3.3. Photothermal and magnetothermal effect on carotid artery inflammation *in vivo*

The macrophages within vessels are derived from monocytes, which can engulf the excessive lipoprotein to form foam cells. It has been demonstrated that the accumulation of foam cells in the subendothelial space is the main pathological process of atherosclerosis [41,42]. It is unavoidable that endothelial cells and SMCs get hurt when treating atherosclerosis by balloon dilatation and/or stent implantation in clinic, which can stimulate the inflammatory response and lead to the accumulation and activation of macrophages within vessels [43]. Activated macrophages surrounding vessels release some cytokines and recruit more inflammation cells, including additional monocytes, T cells neutrophils, which may stimulate SMCs hyperplasia and lead to restenosis of vessels [44,45]. Therefore, the elimination of inflammatory macrophages might prevent the development of atherosclerosis and vessels stenosis effectively. As described above, Apo E ($-/-$) mice were used to make atherosclerosis models. After treated with different measures, they were divided into Control group, Fe_3S_4+PTT group, Fe_3S_4+MHT group, and Fe_3S_4+PTT + MHT group. The representative white light photos of mice in different groups were provided in Figure S4 and local temperatures around left necks were recorded dynamically using an infrared thermal camera. The average temperature of Fe_3S_4+PTT group, Fe_3S_4+MHT group and Fe_3S_4+PTT + MHT group increased to 43.5 °C, 37.8 °C and 49.8 °C, respectively, while that of the control group did not change dramatically (Fig. 7A–E). After 14 days, the left carotid arteries were taken out for HE staining and immunofluorescence staining and the slices were observed under the fluorescence microscope. The results showed that compared with the control group, the number of macrophages infiltrated in the Fe_3S_4+PTT group and Fe_3S_4+MHT group reduced greatly; while the number of macrophages in the Fe_3S_4+PTT + MHT group was the least, which was significantly less than other three groups (Fig. 8A and B). This suggests that the integration of PTT and MHT can ablate inflammatory macrophages
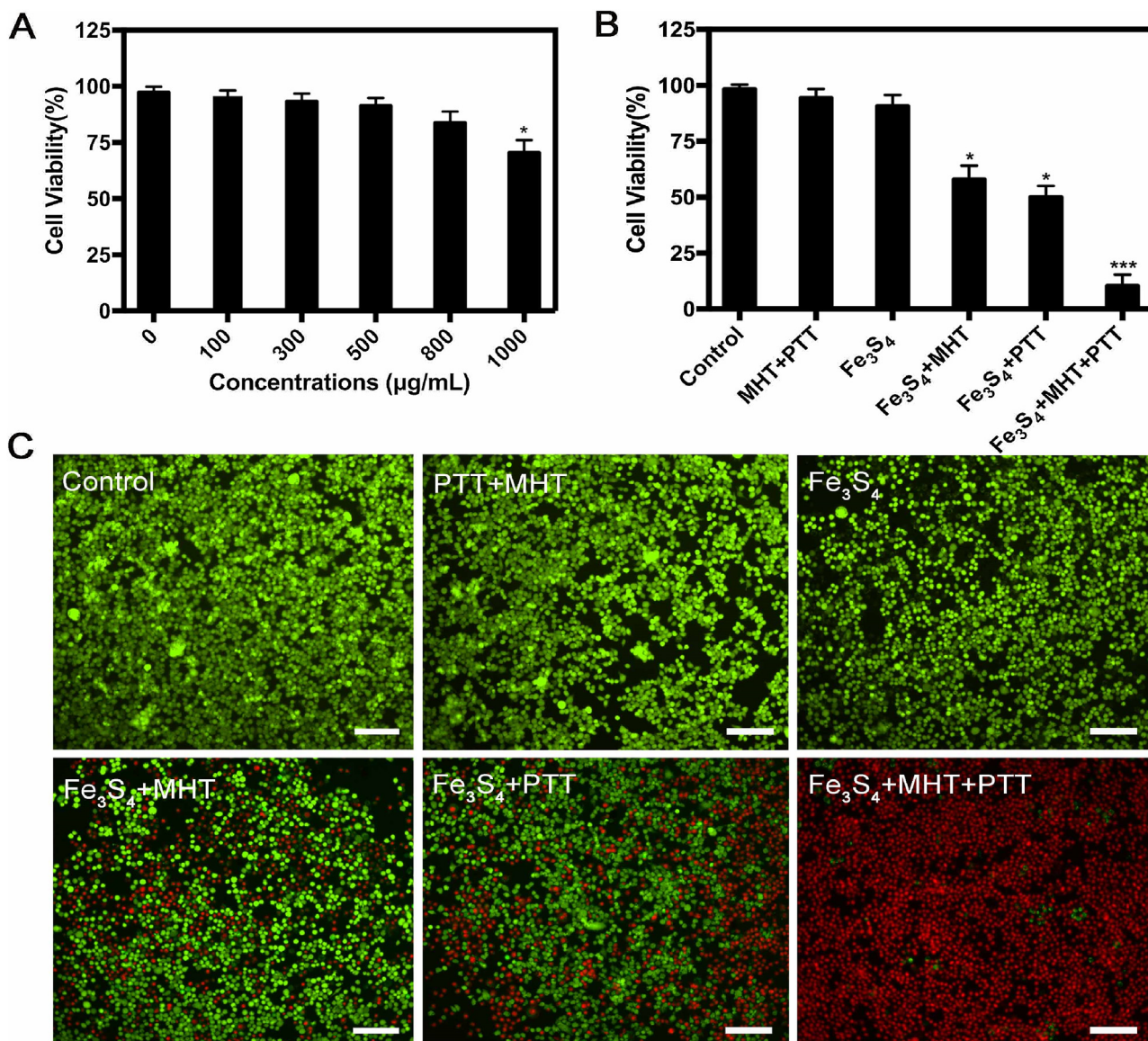
Fig. 5. Cytotoxicity of Fe_3S_4 NPs and its heat effects on macrophages. (A) *in vitro* cell viability of macrophages after incubation with different concentration of Fe_3S_4 NPs. (B) The cell viability of macrophages with or without Fe_3S_4 NPs ($500 \mu g\,mL^{-1}$) after treatment with photothermal therapy (PTT, 808 nm, $0.3\,W/cm^2$), magnetic hyperthermia (MHT, 595 kHz, 14.5 kA) or DUAL (PTT + MHT, both effects) for 5 min respectively. (C) Representative images of live (green) and dead (red) cells with or without Fe_3S_4 NPs ($500 \mu g\,mL^{-1}$) after treatment with PTT, MHT or PTT + MHT respectively. Scale bar: 100 μm. Data are representative of at least three independent experiments.

within vessels effectively. Moreover, HE staining revealed that the average thickness of intima and media in the Fe_3S_4+PTT group and Fe_3S_4+MHT group was much thinner than that of the control group, but the thickness of intima and media of the PTT + MHT group was the thinnest (Fig. 9A and B). This effect can be explained by the promotion of SMC apoptosis and the inhibition of SMC proliferation through eliminating inflammatory macrophages. Therefore, the results suggested that the combination of PTT and MHT of Fe_3S_4 NPs can serve as an effective method to inhibit arterial inflammation and arterial stenosis. However, the optimal concentration of Fe_3S_4 NPs and its corresponding AC magnetic field and laser power need to be further studied. Moreover, its long-term effects and complications still need in-depth exploration.

3.4. Biocompatibility of the Fe_3S_4 NPs

Good biocompatibility is the prerequisite for the research in the living body, the biocompatibility of Fe_3S_4 NPs *in vivo* was tested in addition to the cytotoxicity examination of Fe_3S_4 NPs *in vitro*.

The blood samples of mice in Fe_3S_4 group and the control group were examined at the timepoints of 3 days, 7 days and 14 days. No significant difference was detected in alanine aminotransferase (ALT), aspartate aminotransferase (AST), blood urea nitrogen (BUN) and creatinine (CR), which represent the function of liver and kidney (Fig. 10A–D). The serum biochemical examination also showed that no meaningful changes were found in blood platelet (PLT), D-Dimer, hemoglobin (HGB), total protein (TP) and albumin (ALB), indicating that no adverse effects induced by Fe_3S_4 NPs (Fig. 10E–I). Additionally, the main organs of Fe_3S_4 groups and the control group were excised and then subjected to HE staining. Compared with the control group, no obvious pathological changes such as inflammation, tissue damage and necrosis were observed in the heart, intestine, kidney, lung, liver and spleen of the Fe_3S_4 group mice (Fig. 10J). Besides, the distribution of Fe_3S_4 NPs was also examined by measuring iron concentration. As is shown in Fig. S5, the iron concentrations in major organs increased significantly at the 1st day of injection, especially in liver and kidney, and the concentration nearly recovered to normal level at the 7th day. Those results
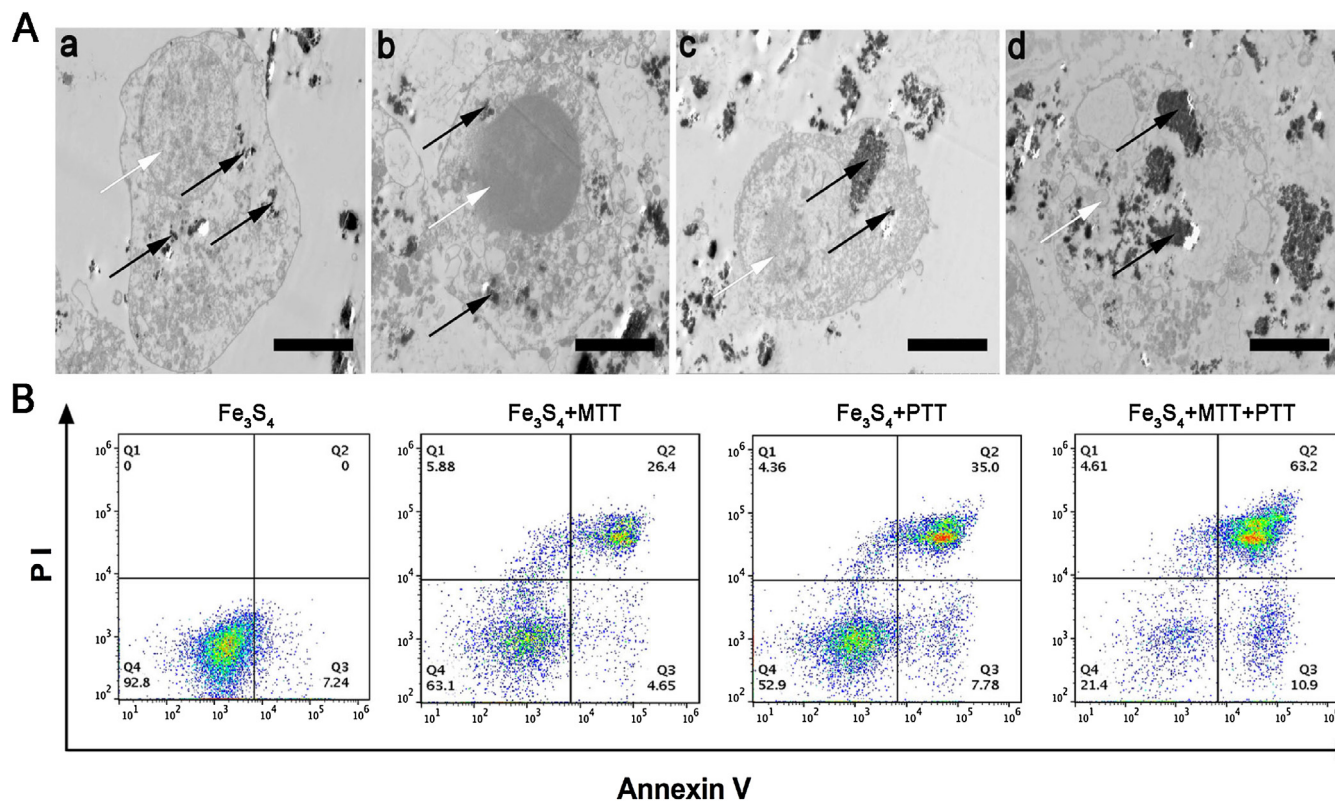
Fig. 6. (A) Representative transmission electron micrographs images of Raw264.7 with Fe_3S_4 NPs after heat treatment. (a) No significant changes were found in Raw264.7 after incubation with Fe_3S_4 NPs ($500 \,\mu g \, mL^{-1}$) for 12 h. (b) Nuclear pyknosis was observed in Raw264.7 after magnetic hyperthermia (MHT, 595 kHz, 14.5 kA) for 5 min. (c) Cell shrinkage and nuclear fragmentation were noticed in Raw264.7 after photothermal therapy (PTT, 808 nm, 0.3 W/cm²) for 5 min. (d) Significant nuclear solubilization and cell lysis were detected after exposed to DUAL (PTT + MHT, both effects) for 5 min simultaneously. White arrows in figures represent the location of the nucleus and black arrows indicate Fe_3S_4 NPs engulfed by macrophages. (B) Flow cytometry analysis of Raw264.7 incubated with Fe_3S_4 NPs ($500 \,\mu g \, mL^{-1}$) and treated with different measures. Scale bar: $5 \,\mu m$.
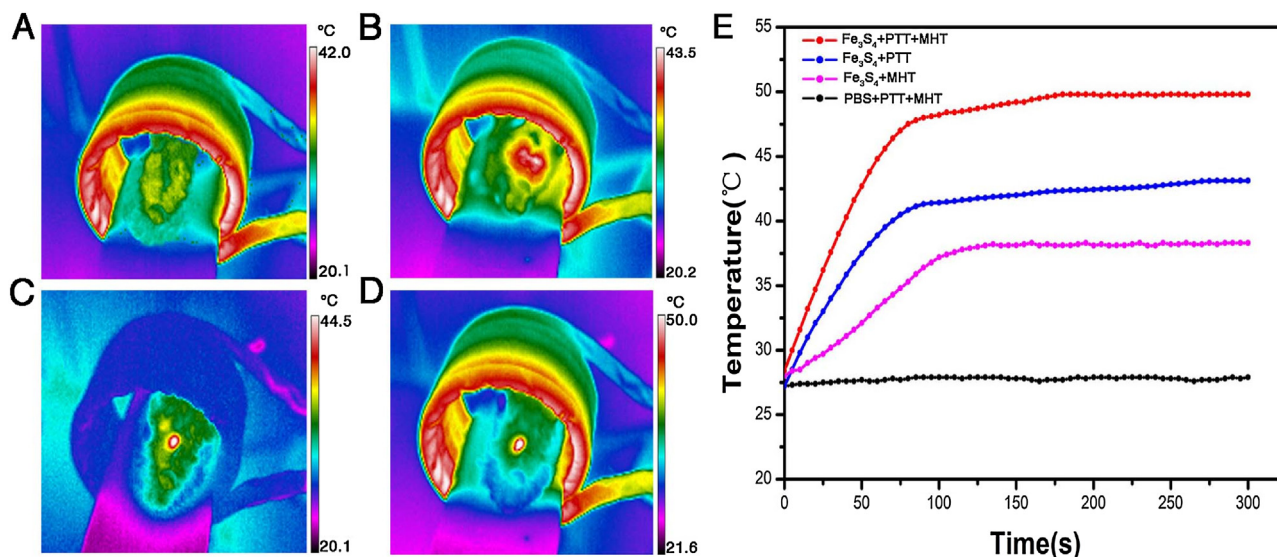

Fig. 7. *In vivo* heat therapy of Fe_3S_4 NPs on mice model. (A) Infrared thermal image of a mouse injected with PBS and treated with DUAL (PTT + MHT, both effects). (B) Infrared thermal image of a mouse injected with Fe_3S_4 NPs and treated with magnetic hyperthermia (MHT, 595 kHz, 14.5 kA). (C) Infrared thermal image of a mouse injected with Fe_3S_4 NPs and treated with photothermal therapy (PTT, 808 nm, 0.3 W/cm²). (D) Infrared thermal image of a mouse injected with Fe_3S_4 NPs and treated with DUAL (PTT + MHT, both effects). (E) Representative temperature changes around left neck of mice at the group of control, Fe_3S_4+MHT, Fe_3S_4+PTT, Fe_3S_4+PTT + MHT respectively. Data are representative of at least three independent experiments.
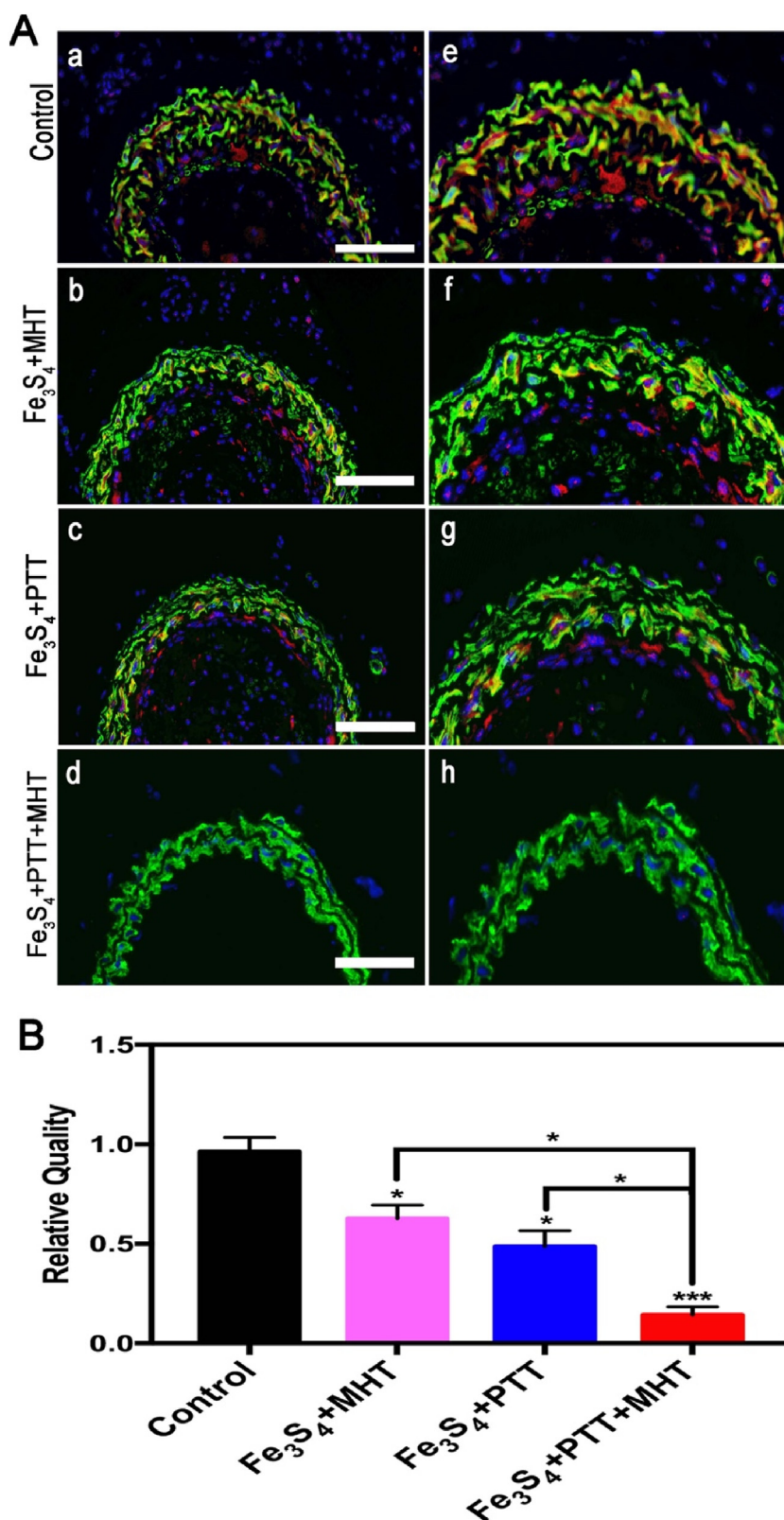
Fig. 8. (A) Representative immunofluorescence images of carotid artery inflammation in mice model. a, b, c and d are representative images of SMA (green) and CD68 (red) co-staining in collar-implanted group mice (Control), collar-implanted group mice with Fe_3S_4 NPs (500 μg ml^{-1}, 100 μL) injection and photothermal therapy (PTT, 808 nm, 0.3 W/cm^2) for 5 min (Fe_3S_4+PTT), collar-implanted group mice with Fe_3S_4 NPs (500 μg ml^{-1}, 100 μL) injection and magnetic hyperthermia (MHT, 595 kHz, 14.5 kA) for 5 min (Fe_3S_4+MHT), collar-implanted group mice with Fe_3S_4 NPs (500 μg ml^{-1}, 100 μL) injection and DUAL (PTT + MHT, both effects) for 5 min (Fe_3S_4 +PTT + MHT) respectively. e, f, g and h are high magnification images of a, b, c and d respectively. (B) Statistics result of the number of macrophages in different groups. Data are representative of at least three independent experiments. Scale bar: 100 μm.
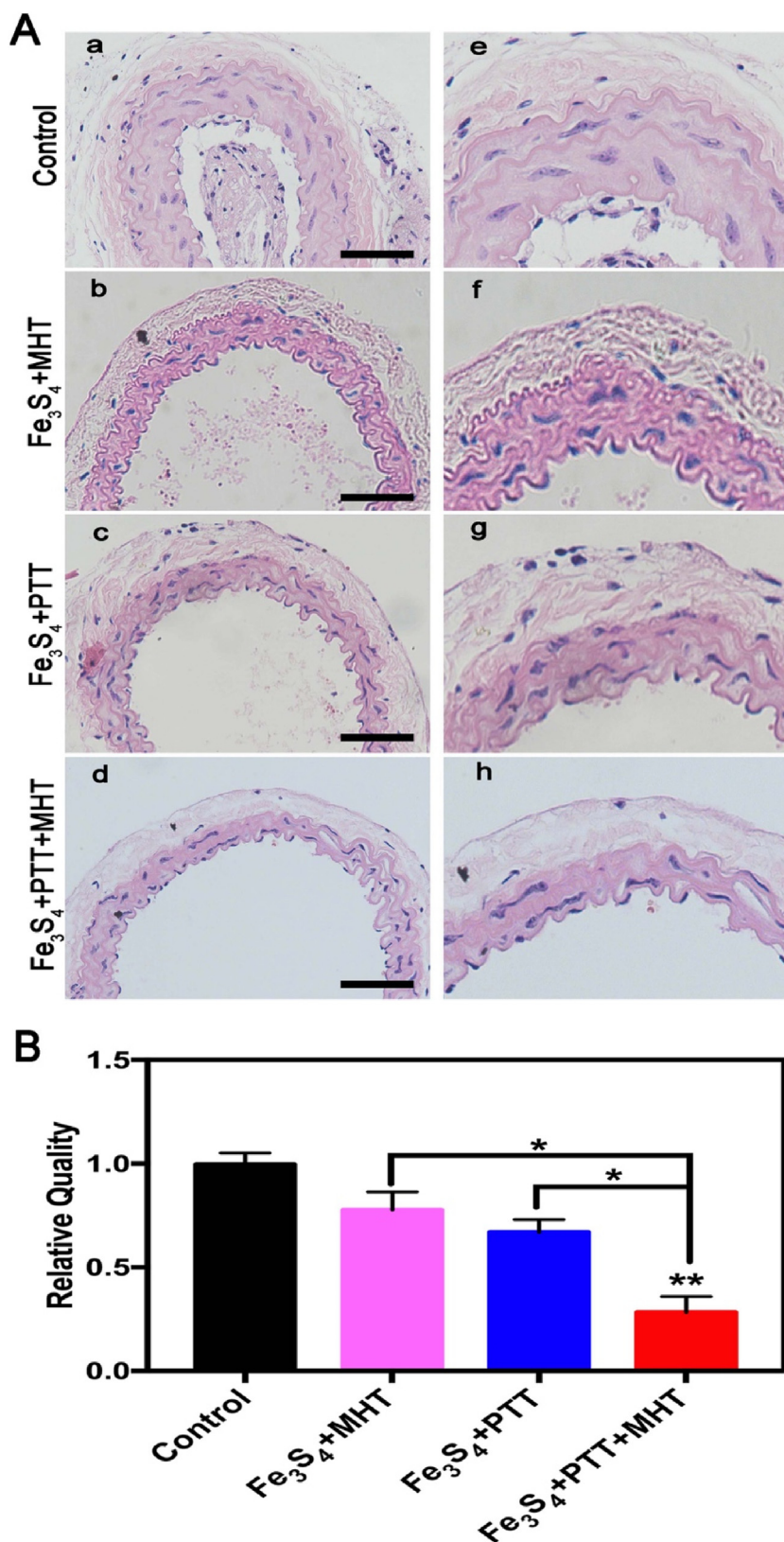
Fig. 9. (A) Representative HE images of carotid artery thickness in mice model. a, b, c and d are the intima and media thickness images of collar-implanted group mice (Control), collar-implanted group mice with Fe_3S_4 NPs (500 μg ml^{-1}, 100 μL) injection and photothermal therapy (PTT, 808 nm at 0.3 W/cm^2) for 5 min (Fe_3S_4+PTT), collar-implanted group mice with Fe_3S_4 NPs (500 μg ml^{-1}, 100 μL) injection and magnetic hyperthermia (MHT, 595 kHz, 14.5 kA) for 5 min (Fe_3S_4+MHT), collar-implanted group mice with Fe_3S_4 NPs (500 μg ml^{-1}, 100 μL) injection and DUAL (PTT + MHT, both effects) for 5 min (Fe_3S_4 +PTT + MHT) respectively. e, f, g and h are high magnification images of a, b, c and d respectively. (B)Statistics result of artery thickness in different groups. Data are representative of at least three independent experiments. Scale bar: 100 μm.
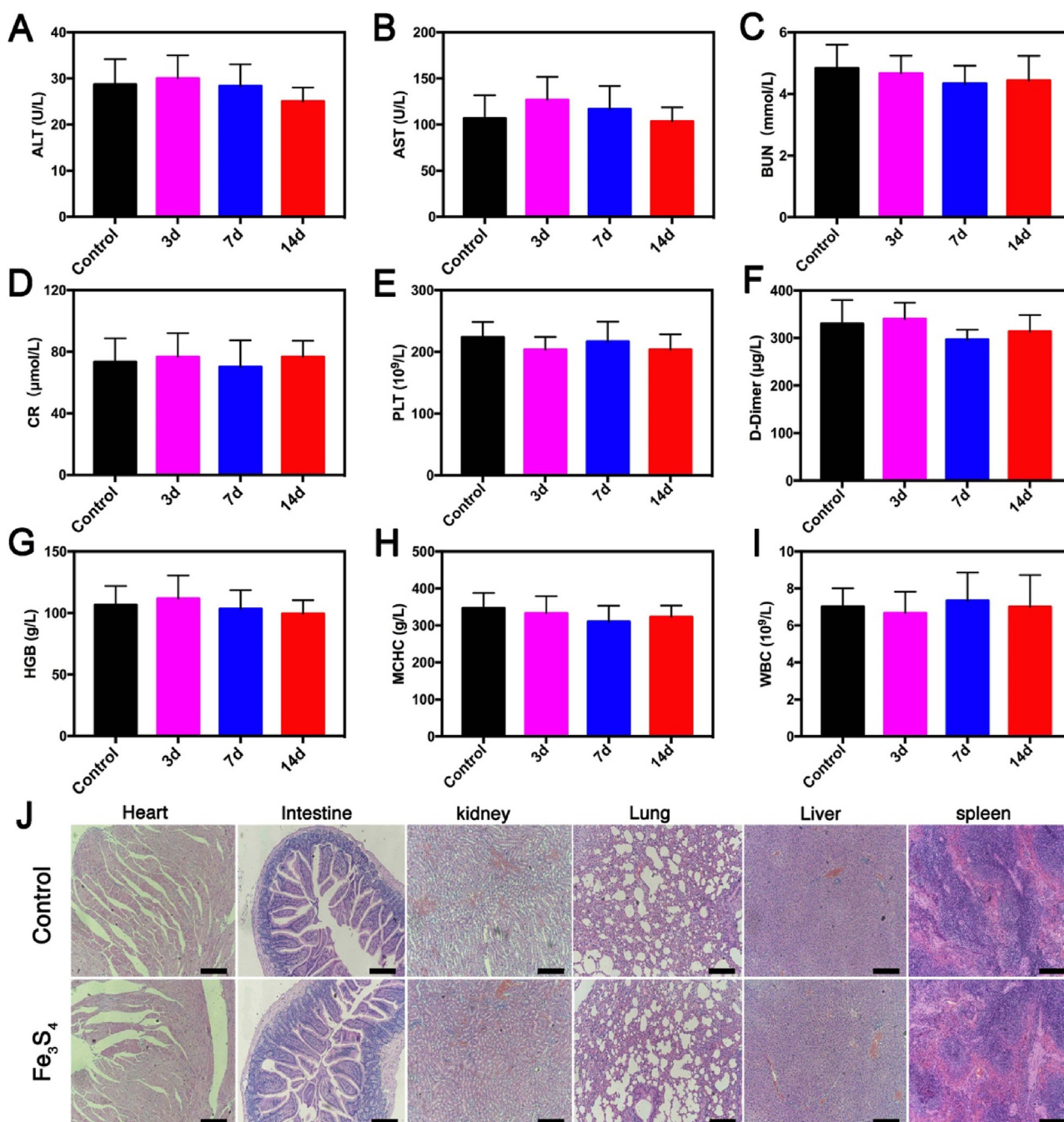
Fig. 10. Biocompatibility assay of Fe_3S_4 NPs *in vivo*. Blood biochemical results of control group and Fe_3S_4 group at different time points (3 days, 7 days, 14 days) after injection, including (A) alanine aminotransferase (ALT), (B) aspartate aminotransferase (AST), (C) blood urea nitrogen (BUN), (D) creatinine (CR), (E) blood platelet (PLT), (F) D-Dimer, (G) hemoglobin (HGB), (H) total protein (TP), (I) albumin (ALB). (J) HE staining results of main visceral organs. No significant changes were observed in heart, intestine, kidney, lung, liver, spleen between control group and Fe_3S_4 groups. Data are representative of at least three independent experiments. Scale bar: 100 μm.

indicated that Fe_3S_4 NPs could be cleared from body in short time, thus reducing its side effect on major organs *in vivo*. Those results illustrate that Fe_3S_4 NPs has no obvious toxic effects and can be safely applied to the living body.

4. Conclusions

In conclusion, Fe_3S_4 NPs were successfully synthesized with high photothermal efficiency and good magnetothermal efficiency. *In vitro* results showed that Fe_3S_4 NPs had superior biocompatibility and great T2 weighted MRI properties and could ablate inflammatory macrophages efficiently with reduced laser power exposure and reduced magnetic field frequency. *In vivo* experiments on Apo E knockout mice suggested that the combination of photothermal therapy and magnetic hyperthermia was effective in eliminating inflammatory macrophages and further inhibiting the formation of atherosclerosis and arterial stenosis. Nevertheless, the optimal therapeutic concentration of Fe_3S_4 NPs and the corresponding AC magnetic strength and laser power were to be further investigated. In conclusion, this work demonstrates that the integration of photothermal therapy and magnetic hyperthermia based on Fe_3S_4 NPs can alleviate inflammatory macrophages effectively, which may provide a new strategy for the treatment of atherosclerosis and arterial stenosis.

Declaration of Competing Interest

The authors declare no conflict of interest.

Acknowledgements

Appendix A. Supplementary data

Supplementary material related to this article can be found, in the online version, at doi:https://doi.org/10.1016/j.apmt.2019.100457.

References

[1] G.B.D.Co.D. Collaborators, Global, regional, and national age-sex specific mortality for 264 causes of death, 1980-2016: a systematic analysis for the Global Burden of Disease Study 2016, Lancet 390 (10100) (2017) 1151–1210.

[2] G.F. Kwan, E.J. Benjamin, I. Tzoulaki, P. Elliott, V. Kontis, M. Ezzati, Worldwide exposures to cardiovascular risk factors and associated health effects: current knowledge and data gaps, Circulation 133 (23) (2016) 2314–2333.

[3] N.V.K. Pothineni, S. Subramany, K. Kuriakose, L.F. Shirazi, F. Romeo, P.K. Shah, J.L. Mehta, Infections, atherosclerosis, and coronary heart disease, Eur. Heart J. 38 (43) (2017) 3195–3201.

[4] J. Frostegard, Immunity, atherosclerosis and cardiovascular disease, BMC Med. 11 (117) (2013) 1–13.

[5] M. Nahrendorf, F.K. Swirski, Neutrophil-macrophage communication in inflammation and atherosclerosis, Science 349 (6245) (2015) 237–238.

[6] T. Yamashita, N. Sasaki, K. Kasahara, K. Hirata, Anti-inflammatory and immune-modulatory therapies for preventing atherosclerotic cardiovascular disease, J. Cardiol. 66 (1) (2015) 1–8.

[7] P.M. Ridker, T.F. Luscher, Anti-inflammatory therapies for cardiovascular disease, Eur. Heart J. 35 (27) (2014) 1782–1791.

[8] W.F. Fearon, D.T. Fearon, Inflammation and cardiovascular disease: role of the interleukin-1 receptor antagonist, Circulation 117 (20) (2008) 2577–2579.

[9] Y.Q. Liu, T. Li, H.S. Ma, D. Zhai, C.J. Deng, J.W. Wang, S.J. Zhuo, J. Chang, C.T. Wu, 3D-printed scaffolds with bioactive elements-induced photothermal effect for bone tumor therapy, Acta Biomater. 73 (2018) 531–546.

[10] N. Yu, J. Li, Z. Wang, S. Yang, Z. Liu, Y. Wang, M. Zhu, D. Wang, Z. Chen, Blue Te nanoneedles with strong NIR photothermal and laser-enhanced anticancer effects as "All-in-One" nanoagents for synergistic thermo-chemotherapy of tumors, Adv. Healthcare Mater. 7 (21) (2018), e1800643.

[11] J. Huang, N. Li, C. Zhang, Z. Meng, Metal-organic framework as a microreactor for in situ fabrication of multifunctional nanocomposites for photothermal-chemotherapy of tumors in vivo, ACS Appl. Mater. Interfaces 10 (45) (2018) 38729–38738.

[12] P. Hu, T. Wu, W. Fan, L. Chen, Y. Liu, D. Ni, W. Bu, J. Shi, Near infrared-assisted Fenton reaction for tumor-specific and mitochondrial DNA-targeted photochemotherapy, Biomaterials 141 (2017) 86–95.

[13] C. Dai, Y. Chen, X. Jing, L. Xiang, D. Yang, H. Lin, Z. Liu, X. Han, R. Wu, Two-dimensional tantalum carbide (MXenes) composite nanosheets for multiple imaging-guided photothermal tumor ablation, ACS Nano 11 (12) (2017) 12696–12712.

[14] X. Zhang, Z. Xi, J.O. Machuki, J. Luo, D. Yang, J. Li, W. Cai, Y. Yang, L. Zhang, J. Tian, K. Guo, Y. Yu, F. Gao, Gold cube-in-Cube based oxygen nanogenerator: a theranostic nanoplatform for modulating tumor microenvironment for precise chemo-phototherapy and multimodal imaging, ACS Nano 13 (5) (2019) 5306–5325.

[15] N. Yu, C. Peng, Z. Wang, Z. Liu, B. Zhu, Z. Yi, M. Zhu, X. Liu, Z. Chen, Dopant-dependent crystallization and photothermal effect of Sb-doped SnO nanoparticles as stable theranostic nanoagents for tumor ablation, Nanoscale 10 (5) (2018) 2542–2554.

[16] C. Fang, P.J. Yan, Z.H. Ren, Y.F. Wang, X.J. Cai, X. Li, G.R. Han, Multifunctional MoO2-ICG nanoplatform for 808nm-mediated synergetic photodynamic/photothermal therapy, Appl. Mater. Today 15 (2019) 472–481.

[17] Q.Q. Yu, Y.M. Han, X.C. Wang, C. Qin, D. Zhai, Z.F. Yi, J. Chang, Y. Xiao, C.T. Wu, Copper silicate hollow microspheres-incorporated scaffolds for chemo-photothermal therapy of melanoma and tissue healing, ACS Nano 12 (3) (2018) 2695–2707.

[18] L. Chang, Y.Q. Liu, C.T. Wu, Copper-doped mesoporous bioactive glass for photothermal enhanced chemotherapy, J. Biomed. Nanotechnol. 14 (4) (2018) 786–794.

[19] K. Deng, Z. Hou, X. Deng, P. Yang, C. Li, J. Lin, Enhanced antitumor efficacy by 808 nm laser-induced synergistic photothermal and photodynamic therapy based on a indocyanine-green-attached W18 O49 nanostructure, Adv. Funct. Mater. 25 (47) (2015) 7280–7290.

[20] J. Lin, S.J. Wang, P. Huang, Z. Wang, S.H. Chen, G. Niu, W.W. Li, J. He, D.X. Cui, G.M. Lu, X.Y. Chen, Z.H. Nie, Photosensitizer-loaded gold vesicles with strong plasmonic coupling effect for imaging-guided photothermal/photodynamic therapy, ACS Nano 7 (6) (2013) 5320–5329.

[21] Y. Wang, X. Liu, G. Deng, J. Sun, H. Yuan, Q. Li, Q. Wang, J. Lu, Se@SiO2-FA-CuS nanocomposites for targeted delivery of DOX and nano selenium in synergistic combination of chemo-photothermal therapy, Nanoscale 10 (6) (2018) 2866–2875.

[22] Bo Li, F.K. Yuan, G.J. He, X.Y. Han, X. Wang, J.B. Qin, Z.X. Guo, X.W. Lu, Q. Wang, Ivan P. Parkin, C.T. Wu, Ultrasmall CuCo2S4 nanocrystals: all-in-one theragnosis nanoplatform with magnetic resonance/near-infrared imaging for efficiently photothermal therapy of tumors, Adv. Funct. Mater. 27 (10) (2017), 160268.

[23] Z.M. Tang, P.R. Zhao, D.L. Ni, Y.Y. Liu, M. Zhang, H. Wang, H. Zhang, H.B. Gao, Z.W. Yao, W.B. Bu, Pyroelectric nanoplatform for NIR-II-triggered photothermal therapy with simultaneous pyroelectric dynamic therapy, Mater. Horiz. 5 (5) (2018) 946–952.

[24] Z.W. Tay, P. Chandrasekharan, A. Chiu-Lam, D.W. Hensley, R. Dhavalikar, X.Y. Zhou, E.Y. Yu, P.W. Goodwill, B. Zheng, C. Rinaldi, S.M. Conolly, Magnetic particle imaging-guided heating in vivo using gradient fields for arbitrary localization of magnetic hyperthermia therapy, ACS Nano 12 (4) (2018) 3699–3713.

[25] Y. Du, X. Liu, Q. Liang, X.J. Liang, J. Tian, Optimization and design of magnetic ferrite nanoparticles with uniform tumor distribution for highly sensitive MRI/MPI performance and improved magnetic hyperthermia therapy, Nano Lett. 19 (6) (2019) 3618–3626.

[26] E. Cazares-Cortes, S. Cabana, C. Boitard, E. Nehlig, N. Griffete, J. Fresnais, C. Wilhelm, A. Abou-Hassan, C. Menager, Recent insights in magnetic hyperthermia: from the "hot-spot" effect for local delivery to combined magneto-photo-thermia using magneto-plasmonic hybrids, Adv. Drug Deliv. Rev. 138 (2019) 233–246.

[27] L.M. Bauer, S.F. Situ, M.A. Griswold, A.C. Samia, High-performance iron oxide nanoparticles for magnetic particle imaging-guided hyperthermia (hMPI), Nanoscale 8 (24) (2016) 12162–12169.

[28] A. Espinosa, R. Di Corato, J. Kolosnjaj-Tabi, P. Flaud, T. Pellegrino, C. Wilhelm, Duality of iron oxide nanoparticles in cancer therapy: amplification of heating efficiency by magnetic hyperthermia and photothermal bimodal treatment, ACS Nano 10 (2) (2016) 2436–2446.

[29] M.H. Li, W.B. Bu, J. Ren, J.B. Li, L. Deng, M.Y. Gao, X.L. Gao, P.J. Wang, Enhanced synergism of thermo-chemotherapy for liver cancer with magnetothermally responsive nanocarriers, Theranostics 8 (3) (2018) 693–709.

[30] Q. Lu, X. Dai, P. Zhang, X. Tan, Y. Zhong, C. Yao, M. Song, G. Song, Z. Zhang, G. Peng, Z. Guo, Y. Ge, K. Zhang, Y. Li, Fe3O4@Au composite magnetic nanoparticles modified with cetuximab for targeted magneto-photothermal therapy of glioma cells, Int. J. Nanomed. 13 (2018) 2491–2505.

[31] A. Curcio, A.K.A. Silva, S. Cabana, A. Espinosa, B. Baptiste, N. Menguy, C. Wilhelm, A. Abou-Hassan, Iron oxide nanoflowers @ CuS hybrids for cancer tri-therapy: interplay of photothermal therapy, magnetic hyperthermia and photodynamic therapy, Theranostics 9 (5) (2019) 1288–1302.

[32] X. Zhang, J. Liu, X. Yang, G. He, B. Li, J. Qin, P.R. Shearing, D.J.L. Brett, J. Hu, X. Lu, CuCo2S4 nanocrystals as a nanoplatform for photothermal therapy of arterial inflammation, Nanoscale 11 (19) (2019) 9733–9742.

[33] J. Qin, Z. Peng, B. Li, K. Ye, Y. Zhang, F. Yuan, X. Yang, L. Huang, J. Hu, X. Lu, Gold nanorods as a theranostic platform for in vitro and in vivo imaging and photothermal therapy of inflammatory macrophages, Nanoscale 7 (33) (2015) 13991–14001.

[34] Z. Peng, J. Qin, B. Li, K. Ye, Y. Zhang, X. Yang, F. Yuan, L. Huang, J. Hu, X. Lu, An effective approach to reduce inflammation and stenosis in carotid artery: polypyrrole nanoparticle-based photothermal therapy, Nanoscale 7 (17) (2015) 7682–7691.

[35] Z.M. Tang, H.L. Zhang, Y.Y. Liu, D.L. Ni, H. Zhang, J.W. Zhang, Z.W. Yao, M.Y. He, J.L. Shi, W.B. Bu, Antiferromagnetic pyrite as the tumor microenvironment-mediated nanoplatform for self-enhanced tumor imaging and therapy, Adv. Mater. 29 (47) (2017), 1701683.

[36] K. Yang, G.B. Yang, L. Chen, L. Cheng, L. Wang, C.C. Ge, Z. Liu, FeS nanoplates as a multifunctional nano-theranostic for magnetic resonance imaging guided photothermal therapy, Biomaterials 38 (2015) 1–9.

[37] Q. Jin, J. Liu, W. Zhu, Z. Dong, Z. Liu, L. Cheng, Albumin-assisted synthesis of ultrasmall FeS2 nanodots for imaging-guided photothermal enhanced photodynamic therapy, ACS Appl. Mater. Interfaces 10 (1) (2018) 332–340.

[38] D.E. Place, T.D. Kanneganti, Cell death-mediated cytokine release and its therapeutic implications, J. Exp. Med. 216 (7) (2019) 1474–1486.

[39] K. Blomgren, M. Leist, L. Groc, Pathological apoptosis in the developing brain, Apoptosis 12 (5) (2007) 993–1010.

[40] S. Ghavami, S. Shojaei, B. Yeganeh, S.R. Ande, J.R. Jangamreddy, M. Mehrpour, J. Christoffersson, W. Chaabane, A.R. Moghadam, H.H. Kashani, M. Hashemi, A.A. Owji, M.J. Łos, Autophagy and apoptosis dysfunction in neurodegenerative disorders, Prog. Neurobiol. 112 (2014) 24–49.

[41] B.G. Childs, D.J. Baker, T. Wijshake, C.A. Conover, J. Campisi, J.M. van Deursen, Senescent intimal foam cells are deleterious at all stages of atherosclerosis, Science 354 (6311) (2016) 472–477.

[42] Michael E. Rosenfeld, Converting smooth muscle cells to macrophage-like cells with KLF4 in atherosclerotic plaques, Nat. Med. 21 (6) (2015) 549–551.

[43] R.L. Morley, A. Sharma, A.D. Horsch, R.J. Hinchliffe, Peripheral artery disease, BMJ 360 (2018) j5842.

[44] G.J. Koelwyn, E.M. Corr, E. Erbay, K.J. Moore, Regulation of macrophage immunometabolism in atherosclerosis, Nat. Immunol. 19 (6) (2018) 526–537.

[45] A. Warnatsch, M. Ioannou, Q. Wang, V. Papayannopoulos, Inflammation. Neutrophil extracellular traps license macrophages for cytokine production in atherosclerosis, Science 349 (6245) (2015) 316–320.